Characterizing the Controllable Entry States and Reachable Sites for Planetary Landing

Joel Benito* and Kenneth D. Mease†
University of California, Irvine, 92697-3975

Understanding the envelope of entry trajectories that a given planetary lander is capable of flying can be important aid for mission analysis and design. We consider two characteristics of this envelope: (i) the set of states reachable from a given entry state, and (ii) the set of entry states controllable to a given final state. Precise definitions of these sets are given and methods for computing them are presented. To illustrate their use, the sets are employed to characterize the Mars entry of two vehicle configurations, a low lift-to-drag ratio (L/D) capsule and a mid L/D ellipsled. The effect of changing the parachute deployment speed from Mach 2 to Mach 5 is also analyzed.

I. Introduction

For planetary landing mission analysis and design, it is beneficial to characterize the envelope of trajectories that a given planetary lander is capable of flying. In particular, two characteristics of this envelope are the focus of our attention: (i) the set of states reachable from a given entry state, and (ii) the set of entry states controllable to a given final state. The objectives of this paper are to define the reachable set (RS) and the controllable set (CS), present methods for their computation, and illustrate the use of these sets via a detailed application to Mars entry for two different vehicle configurations.

Reachable and controllable sets are established concepts in mathematical systems theory; see for example Sontag[1]. We adapt the standard definitions to accommodate the particular features of entry flight – the boundary conditions and the path and control constraints. The landing footprint (see Saraf et al.[2] and references therein), a more familiar concept in flight mechanics, can be derived from the reachable set. The landing footprint is a two-dimensional set, typically parameterized by longitude and latitude. The RS is a six-dimensional set parameterized by all the translational state variables for the entry vehicle. Using spherical coordinates for position and velocity as we do, two of the position coordinates are longitude and latitude. The landing footprint is, in a sense, a projection of the RS onto the longitude-latitude plane. Keeping track of the full translational state for the points that can be reached by a lander is important when state variables in addition to longitude and latitude are of interest. For example, there may be multiple points in the RS with the same longitude and latitude; the one of most interest might be the one with the highest altitude for the reason given in the following paragraph.

Certain future Mars missions are pushing entry, descent, and landing (EDL) technology to accommodate higher accuracy, higher elevation landings[3]. To date, Mars landings have been at sites with below -1.4 km MOLA (Mars Orbiter Laser Altimeter) elevation. To reach much of the Ancient Highlands, the majority of the southern hemisphere, requires landing at + 2-3 km MOLA elevations. The Mars Science Laboratory (MSL) mission, to be launched in 2009, is scheduled to land in the southern hemisphere, at +1.6 km MOLA elevation. All previous missions to Mars have had unguided entries with landing errors only guaranteed to be on the order of 100 km. MSL will have a guided entry and is designed to land within 10 km of the desired site. The MSL capsule has an off-axis center of gravity, providing a small amount of lift with which to modify the flight path to compensate for off-nominal atmospheric and vehicle properties. High elevation landing sites are especially challenging because the parachute deployment altitude has to be higher also. Although there exist nominal trajectories that meet the requirements, if they involve lofting in the final entry phase, the amount of lift available to compensate for off-nominal conditions may be less than needed. Some algorithms have been developed[4,5] that provide reference trajectories that preserve control authority to correct for errors during the final entry phase.

The RS and CS for Mars entry will be characterized for two vehicle configurations, an MSL-type capsule and an ellipsled, and for two parachute deployment speeds (Mach 2 and Mach 5). The RS and CS will be used to

* Graduate Student, Mechanical and Aerospace Engineering Department.
† Professor, Mechanical and Aerospace Engineering Department.

characterize the entry problem and the impact of the deployment speed and vehicle L/D on the entry capability. The trajectory optimization program GESOP[6] will be used to compute key points in the RS and CS. Trajectories are optimized to have high altitude parachute deployment, yet maintain high control authority throughout the trajectory to ensure high deployment accuracy. The lateral motion as well as the longitudinal motion is considered.

II. Entry Problem Formulation

A. Equations of Motion

The equations of motion of an entry vehicle defined with respect to a planet-fixed coordinate frame are shown in Eq. 1[7]

$$\begin{aligned}
\dot{r} &= V\sin\gamma \\
\dot{\theta} &= \frac{V}{r}\frac{\cos\gamma\cos\psi}{\cos\phi} \\
\dot{\phi} &= \frac{V}{r}\cos\gamma\sin\psi \\
\dot{V} &= -D - g\sin\gamma \\
\dot{\gamma} &= \frac{1}{V}\left[L\cos\sigma - \left(g - \frac{V^2}{r}\right)\cos\gamma\right] + C_\gamma \\
\dot{\psi} &= -\frac{1}{V\cos\gamma}\left(L\sin\sigma + \frac{V^2}{r}\cos^2\gamma\cos\psi\tan\phi\right) + C_\psi
\end{aligned} \tag{1}$$

where θ is the longitude, ϕ is the latitude, r is the distance from the center of the planet to the vehicle center of mass, ψ is the heading angle with $\psi = 0$ as due east and $\psi = 90$ deg as due North, V is the velocity and γ is the flight path angle. L and D are the lift and drag accelerations, defined by

$$\begin{aligned}
L &= \frac{1}{2}\rho V^2\frac{S}{m}C_L \\
D &= \frac{1}{2}\rho V^2\frac{S}{m}C_D
\end{aligned} \tag{2}$$

The drag and lift coefficients C_D and C_L are functions of the Mach number; S is the reference area; m is the vehicle mass; and ρ is the atmospheric density. g is the gravitational acceleration. The terms C_ψ and C_γ are the Coriolis accelerations due to planet rotation and are given by

$$\begin{aligned}
C_\psi &= 2\omega_p\left(\tan\gamma\sin\psi\cos\phi - \sin\phi\right) \\
C_\gamma &= 2\omega_p\cos\psi\cos\phi
\end{aligned} \tag{3}$$

where ω_p is the planet angular rate.

B. Trajectory Metrics

Trajectory length is defined by

$$S = \int_{t_0}^{t_f} V\cos\gamma\, dt \tag{4}$$

which corresponds to the horizontal distance traveled by the vehicle.

It is of special interest to deploy the parachute at high altitudes, which is challenging due to the decreased atmospheric density at the desired deployment altitudes. The altitude dynamics are

$$\ddot{h} = -g - D\sin\gamma + \frac{V^2}{r}\cos^2\gamma + L\cos\gamma\cos\sigma + V\cos\gamma C_\gamma \tag{5}$$

The vehicle is controlled by rotating the lift vector around the velocity vector. The vertical component of lift $L\cos\gamma$ is the altitude control authority, which should be as high as possible during the entry, especially close to the deployment point when the velocity is low. $L\cos\gamma$ can be increased in different ways, although they all effectively limit a lofting motion towards the end, which is undesirable because it decreases both L and $\cos\gamma$. More details will be presented in Sections IV and V.

C. Vehicle Model

The geometry of an MSL-type capsule[8] is a double-cone, with an aeroshell forebody shape of a 70 deg sphere-cone. This geometry can provide a lift-to-drag ratio (L/D) of about 0.25. An alternative configuration to the Viking-type double-cone is the ellipsled vehicle[8]. The ellipsled is a geometry formed by a spheroid extending into a cylinder, an elliptically blunted cylinder. This configuration can provide an L/D as high as 0.4. Fig. 1 shows the MSL and ellipsled configurations.

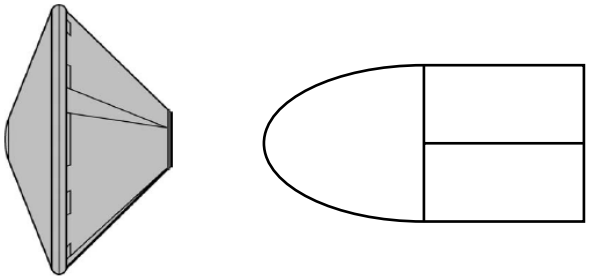

Fig 1. MSL and ellipsled configurations

The constraints described in the remainder of this subsection apply to both vehicle configurations. The control is limited to $|\sigma| \le 90$ deg. Due to limitations in the reaction control system, the bank rate and bank accelerations are limited to $|\dot{\sigma}| \le 20$ deg/s and $|\ddot{\sigma}| \le 5$ deg/s^2.

There are path constraints on heat rate, dynamic pressure and total acceleration. Convective heat rate ($\dot{Q}$) can be approximated at the stagnation point by the Sutton-Graves equation[9]

$$\dot{Q} = k_q \left(\frac{\rho}{r_n}\right)^N V^M \tag{6}$$

where N=0.5, M=3, ρ is the atmospheric density and r_n is the nose radius of the capsule. The values of k_q are shown in Table 1. The expression for dynamic pressure ($\bar{q}$) is shown in Eq. 7, and the expression of the total acceleration (a) due to aerodynamic forces is shown in Eq. 8. The vehicle should not violate the constraints $\dot{Q} \le \dot{Q}_{\max}$, $\bar{q} \le \bar{q}_{\max}$ and $a \le a_{\max}$.

$$\bar{q} = \frac{1}{2}\rho V^2 \tag{7}$$

$$a = \sqrt{D^2 + L^2} \tag{8}$$

For the results in this paper the lift and drag coefficients are assumed to be constant with the Mach number. The parameters of the vehicles used in the simulations presented in this paper are shown in Table 2.

Planet	k_q
Earth	1.74153e-4
Mars	1.90270e-4

Table 1. Sutton-Graves equation coefficients

	MSL-type	Ellipsled	Units
C_D	1.45	1.92	-
C_L	0.36	0.62	-
LoD	0.248	0.323	-
m	2804	3000	kg
S	15.9	15.9	m^2
r_n	0.66	1	m

Table 2. Vehicle parameters

D. Atmospheric and Planetary Models

The atmospheric density ρ is approximated by an exponential function:

$$\rho = \rho_0 \exp\left(-h/h_s\right) \tag{9}$$

where ρ_0 is the density on the surface of the planet, h is the altitude and h_s is the scale-height. For the results in this paper the planet is assumed to be spherical with a surface radius r_p, and hence $h = r - r_p$. Given that in this paper the aerodynamic coefficients are taken constant with the Mach number, the speed of sound can be modeled only for low altitudes since the Mach number is only needed for the definition of the constraints of the parachute. For low altitudes the speed of sound can be modeled by a constant velocity V_s. The gravitational acceleration is modeled by $g = \mu / r^2$, where μ is the planet gravitational constant. The numerical values of the planet parameters used in this paper for Mars are shown in Table 3.

Parameter	Value	Units
r_p	3.3866E+06	m
μ	4.284E+13	m^3/s^2
ρ_0	0.0158	kg/m^3
h_s	9354.5	m
V_s	220	m/s
ω_p	7.095e-5	rad/s

Table 3. Martian parameters

The trajectory computed with the nominal entry state, vehicle and planet models that brings the vehicle to the target deployment state is called the nominal trajectory or nominal case. In the presence of uncertainty in the atmospheric and planet models the trajectories are dispersed trajectories or dispersed cases.

E. Parachute Deployment Constraints

Current parachute technology is derived from the Viking-era[3]. The selected parachute configuration is the Disk-Gap-Band, which allows deployment at Mach numbers up to 2.1 and dynamic pressures up to 800 Pa. An increase of the parachute deployment limits in the Mach number and dynamic pressure would allow for a higher altitude parachute deployment and increased control authority during the last part of the entry. Inflatable aerodynamic decelerators[10] are being studied to increase the deployment velocity up to Mach 5.

The parachute deployment constraints are limits in the dynamic pressure and the Mach number. The current supersonic Disk-Gap-Band parachute technology[3] deploys the parachute around Mach 2, and the constraints are shown in Table 4. The parachute deployment constraints form the parachute box, or set of all allowable deployment altitude-velocity pairs for a given atmospheric model. The parachute box for the Disk-Gap-Band parachute technology is shown in Fig. 2.

Parameter	Min. value	Max. value	Units
Mach	1.4	2.2	-
$\bar{q}$	300	850	Pa
h	6	-	km

Table 4. Disk-gap-bank parachute deployment constraints

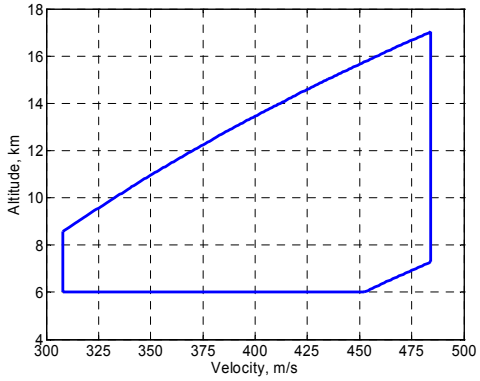

Fig. 2. Disk-Gap-Band Parachute Box

Supersonic decelerators that can be deployed at higher Mach numbers are being studied, like the inflatable aerodynamic decelerators (IADs)[10]. Deployment at higher velocities ensures a higher deployment altitude and increased lift (and therefore increased control authority). In this paper, simulations with two different deployment speeds are studied: Mach 2 and Mach 5.

F. Simulation Environment

The trajectories presented in this paper have been obtained using the Graphical Environment for Simulation and Optimization (GESOP)[6]. GESOP is a trajectory optimization program. The optimization technique used for this paper is the direct multiple shooting method PROMIS. GESOP has an interface to input the dynamics, the constraints and the cost function using MATLAB's Simulink. Once the system has been modeled in Simulink, it is compiled and then GESOP is launched for the optimization.

III. Reachable and Controllable Sets

In this section we define two important sets: (i) the Reachable Set from a specified entry state and (ii) the Controllable Set to a specified parachute deployment longitude and latitude. Reachable and controllable sets are concepts from systems theory, see for example Ref. 1. The standard definitions are modified as needed for the entry guidance context. In preparation for defining the reachable and controllable sets, several other sets are first defined.

The coordinates of the 6-dimensional vehicle translational state are $x = [r, \theta, \phi, V, \gamma, \psi]^T$. The state can take values in the set $\mathrm{X} \subset \Re^6$ defined by

$$\mathrm{X} = \left\{ \begin{matrix} x \in \Re^6 : r \in [r_{\min}, r_{\max}], \theta \in [\theta_{\min}, \theta_{\max}], \phi \in [\phi_{\min}, \phi_{\max}], \\ V \in [V_{\max}, V_{\min}], \gamma \in [\gamma_{\min}, \gamma_{\max}], \psi \in [\psi_{\min}, \psi_{\max}] \end{matrix} \right\} \tag{10}$$

The solution to the equations of motion, Eq. 1, at time t is expressed by the nonlinear transition map

$$x(t) = \mathrm{T}[t, x_0; \sigma[0,t]] \tag{11}$$

indicating the dependence of $x(t)$ on the elapsed time t, the bank angle profile for the time-interval 0 to t, denoted by $\sigma[0,t]$, and the initial condition $x(0) = x_0$. Because the dynamics are time independent, the initial time is always taken to be zero, without loss of generality. The transition map also depends on the particular force models employed, but because we are not investigating the impact of modeling errors in this paper, our notation does not explicitly indicate the model dependence. The set $U(t)$ of admissible σ control profiles is defined by

$$U(t) = \left\{ \sigma \in C^2[0,t] : \sigma(\tau) \in [\sigma_{\min}, \sigma_{\max}], |\dot{\sigma}(\tau)| \le \dot{\sigma}_{\max}, |\ddot{\sigma}(\tau)| \le \ddot{\sigma}_{\max}, \forall \tau \in [0,t] \right\} \tag{12}$$

where $C^2[0,t]$ denotes the set of continuous functions with continuous first and second derivatives on the interval $[0,t]$. Let $P \subset \mathrm{X}$ denote the set of states that do not violate the path constraints on heat rate, acceleration and dynamic pressure, defined by

$$P = \left\{ x \in \mathrm{X} : \dot{Q}(x) \le \dot{Q}_{\max},\ \overline{q}(x) \le \overline{q}_{\max},\ a(x) \le a_{\max} \right\} \tag{13}$$

The deployment set $D \subset \mathrm{X}$, the set of acceptable parachute deployment states, is defined by

$$D = \left\{ x \in \mathrm{X} : M(x) \in \left[M_{\min}, M_{\max}\right],\ \overline{q}(x) \in \left[\overline{q}_{\min}, \overline{q}_{\max}\right],\ h(x) \ge h_{\min} \right\} \tag{14}$$

A feasible trajectory is a trajectory that is generated by an admissible control profile, does not violate the path constraints, and has a final state in *D*. The Reachable Set (RS) $RS(x_0) \subset D$ is the set of states that can be reached by feasible trajectories from the entry state x_0, and is defined by

$$RS(x_0) = \left\{ x \in D : \exists\, t_f > 0 \text{ and } \sigma\left[0,t_f\right] \in U(t_f) \text{ s.t. } x = T\left[t_f, x_0; \sigma\left[0,t_f\right]\right] \text{ and } \forall t \in \left[0,t_f\right],\ T\left[t, x_0; \sigma[0,t]\right] \in P \right\} \tag{15}$$

The Reachable Footprint (RFP) is derived from the $RS(x_0)$ as follows

$$RFP(x_0) = \left\{ (\theta,\phi) : \exists x \in RS(x_0) \text{ s.t. } \Pi(x) = (\theta,\phi) \right\} \tag{16}$$

where the operator $\Pi(x) = \Pi\left(\left[r,\theta,\phi,V,\gamma,\psi\right]^T\right) = (\theta,\phi)$ extracts the 2nd and 3rd variables, longitude and latitude, from the state vector. For each value of $(\theta,\phi) \in RFP(x_0)$ there exists at least one value of $x \in RS(x_0)$. To define the feasible set of entry states, we first limit the states we consider to the subset $X_E \subset X$ defined by

$$X_E = \left\{ x \in X : h(x) = h_E;\ V(x) \in \left[\underline{V}_E, \overline{V}_E\right],\ \psi(x) \in \left[\underline{\psi}_E, \overline{\psi}_E\right] \right\} \tag{17}$$

where the underbar denotes minimum and the overbar maximum. Traditionally, $h_E = 120\ km$. The entry speed range and the heading angle range are dictated by the approach trajectory. The Controllable Set (CS) $CS(\theta_f,\phi_f)$ is the set of states from which there exists a feasible trajectory to a specified deployment longitude and latitude pair (θ_f,ϕ_f), and it is given by

$$CS(\theta_f,\phi_f) = \left\{ \begin{array}{l} x_0 \in X_E : \exists\, t_f > 0 \text{ and } \sigma\left[0,t_f\right] \in U(t_f) \text{ s.t. } \Pi\left(T\left[t_f, x_0; \sigma[0,t_f]\right]\right) = (\theta_f,\phi_f) \text{ and} \\ \forall t \in \left[0,t_f\right],\ T\left[t, x_0; \sigma[0,t]\right] \in P \end{array} \right\} \tag{18}$$

The Controllable Footprint (CFP) is derived from $CS(\theta_f,\phi_f)$ as defined by

$$CFP(\theta_f,\phi_f) = \left\{ (\theta,\phi) : \exists x \in CS(\theta_f,\phi_f) \text{ s.t. } \Pi(x) = (\theta,\phi) \right\} \tag{19}$$

IV. Reachable Sets

A. Computation of the Reachable Set

Since for each $(\theta,\phi) \in RFP(x_0)$ there are typically multiple feasible entry trajectories, given the option to choose a trajectory we are interested in the trajectories with maximum deployment altitude and high control authority. The trajectories are obtained by solving an optimization problem. The set formed by these optimal trajectories is a subset of the RS that will be referred to simply as RS. This subset is of greatest interest, the RFP for the full RS can be derived from it, and it is easier to compute than the full RS. The boundary conditions for the optimization problem

solved for each of the trajectories are shown in Table 5; the initial state and the deployment velocity and trajectory lengths are specified. The final time t_f is free.

Variable	Value
$x(0)$	x_0
$V(t_f)$	V_d
$S(t_f)$	S_d

Table 5. Boundary constraints

The entry state x_0 is shown in Table 6 for the MSL vehicle and in Table 7 for the ellipsled vehicle, along with the minimum and maximum values allowed during entry, which are the path constraints. No limits in heat rate, dynamic pressure and acceleration have been set; although the maximum values of these variables will be examined.

State Variable	Initial Value	Min. Value	Max. Value	Units
r	3522.2	r_p	3522.2	km
θ	-74.73192	-180	180	deg
ϕ	-43.7513	-90	90	deg
V	5433.5	0	5500	m/s
γ	-15.76793	-45	$\gamma_{\max}$	deg
ψ	15.634524	-90	90	deg

Table 6. Entry state for MSL

State Variable	Initial Value	Min. Value	Max. Value	Units
r	3522.2	r_p	3522.2	km
θ	-74.73192	-180	180	deg
ϕ	-43.7513	-90	90	deg
V	5650	0	5800	m/s
γ	-13.0	-45	$\gamma_{\max}$	deg
ψ	15.634524	-90	90	deg

Table 7. Entry State for ellipsled

For the results presented in this paper the parachute is deployed at a fixed velocity. This deployment condition may not be the one that provides the highest deployment altitude for all trajectories, but if it is chosen on the high side of the allowable deployment velocities, the control authority will be high. As shown in Refs. 4-5 this choice provides higher deployment altitudes and horizontal accuracy in the presence of uncertainties. The deployment velocity is set to $V_d = 445\ m/s$ for Mach 2 deployment and $V_d = 1100\ m/s$ for Mach 5 deployment.

S_d is the desired trajectory length, which will be changed to form the edges of the RFP. S_d is increased and decreased until the required trajectory length is unreachable, marking the edge of the RFP.

The trajectories are constrained via a cost function to have high control authority, as explained in Refs. 4-5, to increase the deployment altitude control authority. It is shown in Ref. 4 that limiting the maximum value of γ to $\gamma_{\max}$ is an effective way of limiting the lofting motion and increase the control authority. Ref. 5 includes a term in the cost function to increase the deployment flight path angle, which decreases the lofting motion. This term works better than including the term $\int L\cos\gamma\, dt$ in the cost function, which can provide undesirable results since lift is maximized when the altitude is minimized. Finally, the deployment altitude will be maximized by including the deployment altitude term in cost function shown in Eq. 20 (Ref. 5).

$$J = k_\gamma\left[\gamma_f - \gamma(t_f)\right]^2 - h(t_f) \tag{20}$$

For the two vehicles, the parameters used in the optimization are shown in Table 8.

Variable	MSL Mach 2	MSL Mach 5	Ellipsled Mach 2	Ellipsled Mach 5
k_γ	3.0e5	3.0e5	3.0e5	1.0e7
γ_f	-0.08 rad	-0.15 rad	0.0 rad	0.0 rad
$\gamma_{\max}$	free	free	2.0 deg	2.0 deg

Table 8. Optimization Parameters

The maximum value of the flight path angle is limited to $\gamma_{\max} = 2.0\,\text{deg}$ in the cases in which the vehicle has enough control authority to have a high loft towards the end of the trajectory and thus a decreased control authority.

B. Characterization of the RS of a Nominal MSL-Type Mission

In the nominal MSL mission, the parachute is deployed at Mach 2. The nominal RFP is shown in Fig. 3. The RFP is 171 km long in downrange and 51 km wide in crossrange. Fig. 4 presents the deployment altitude profiles.

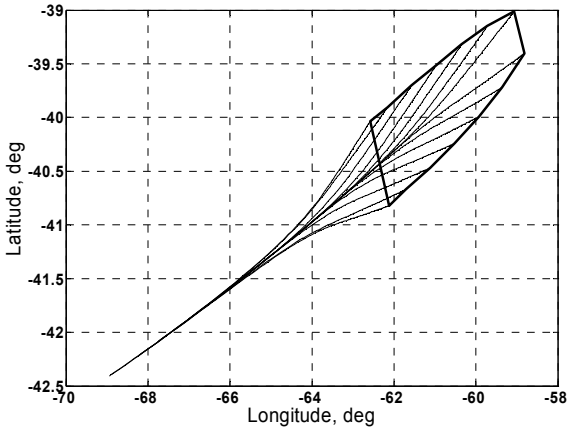

Fig. 3. Nominal RFP

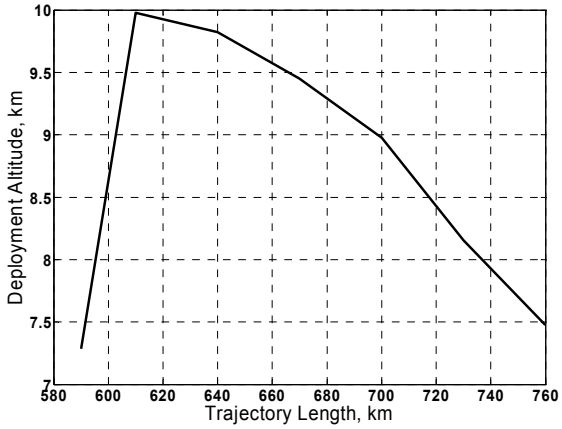

Fig. 4. Deployment altitude

Fig. 4 shows how the edges of the footprint have the lowest deployment altitude. When most of the control effort is placed in minimizing or maximizing the downrange, there is not much left to reach high deployment altitudes. Fig. 5 shows the 3D trajectories that form the RS. To reach high downrange the vehicle has to loft towards the end. Fig. 6 shows the maximum heat rates; for the shorter trajectories where the energy has to be dissipated in a shorter time, the maximum achieved heat rates are higher.

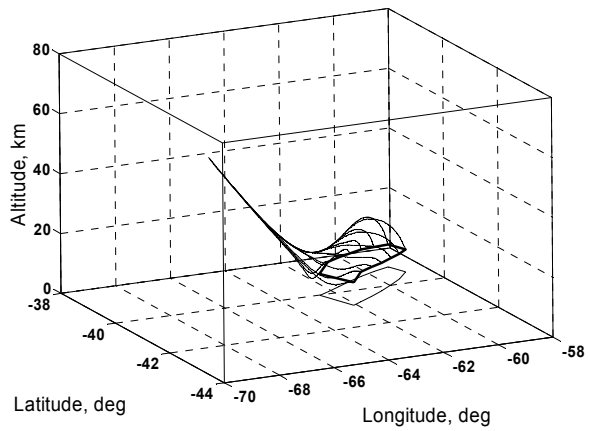

Fig. 5. 3D trajectories

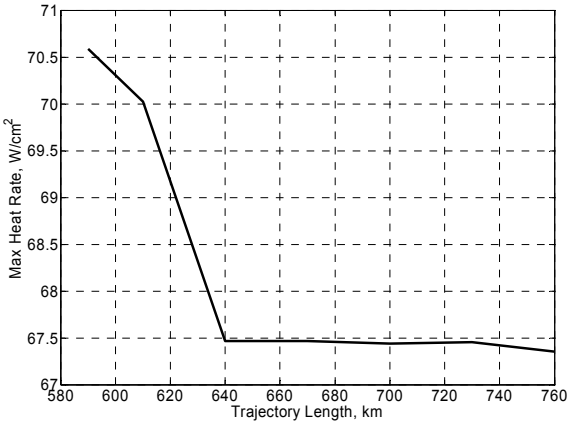

Fig. 6. Max heat rate

These plots show the importance of placing the deployment site in the center of the RFP: the maximum deployment altitude is the highest, the maximum heat rate is low, there is no lofting close to the deployment point and hence no loss in control authority, and the control does not need to be saturated for most of the entry to achieve the required downrange, leaving room for trajectory corrections. Another criterion to place the target deployment point in the center of the RFP is based on flexibility to accommodate dispersions in the entry state. The entry guidance algorithm has not only to deal with uncertainty in the atmospheric and aerodynamic models, but also with an off-nominal entry point; changes in the entry state affect the characteristics of the RS. Fig. 7 shows the RFP for

changes in the entry flight path angle of 0.5 deg. Table 9 shows the approximate size of the footprints, the width measured at the point of minimum trajectory length. Fig. 8 shows the deployment altitude and Fig. 9 the maximum heat rate.

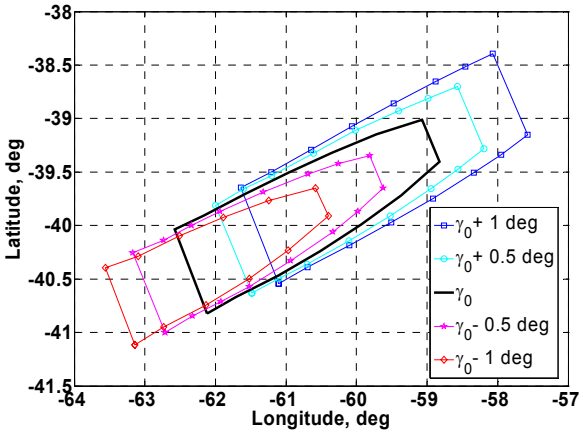

Fig. 7. RFPs for changes in the entry flight path angle

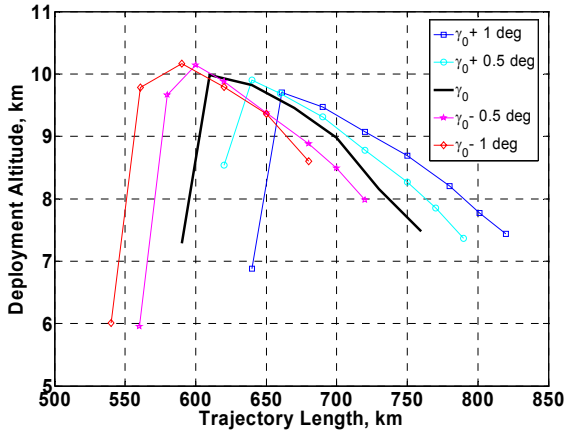

Fig. 8. Deployment altitude for changes in the entry flight path angle

Steep entry flight path angle not only brings the RFP closer to the entry point but also shrinks it in size. The deployment altitudes do not change significantly with the change in entry flight path angle; the maximum deployment altitudes are achieved in the near side of the center of the footprint. The maximum heat rates achieved during entry are, however, significantly affected. The trajectories with the steepest entry flight path angle have the highest maximum heat rate, as expected.

	Length (km)	Width (km)	Area (km^2)
$\gamma_0 + 1$ deg	180	59	10620
$\gamma_0 + 0.5$ deg	174	54	9396
γ_0	171	51	8721
$\gamma_0 - 0.5$ deg	161	48	7768
$\gamma_0 - 1$ deg	142	46	6532

Table 9. Approximated RFP size

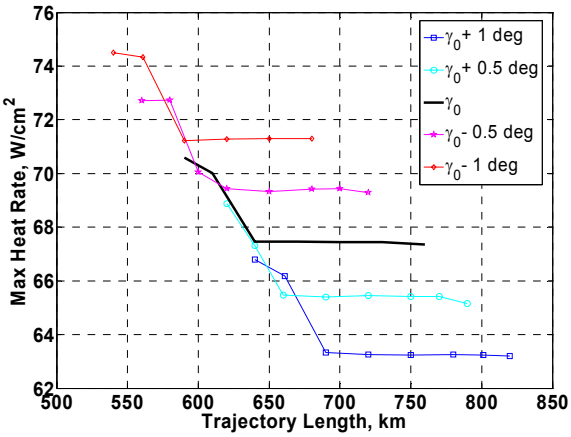

Fig. 9. Maximum heat rate for changes in the entry flight path angle

Fig, 10 shows the RFP for changes in the entry heading angle. The convention for heading angle used in these simulations is counter-clockwise from East, so positive increments from ψ_0 turn the RFP towards the North, and negative increments towards the South. The longitudinal variables do not change with respect to the nominal case, and they are same than Figs. 7-12.

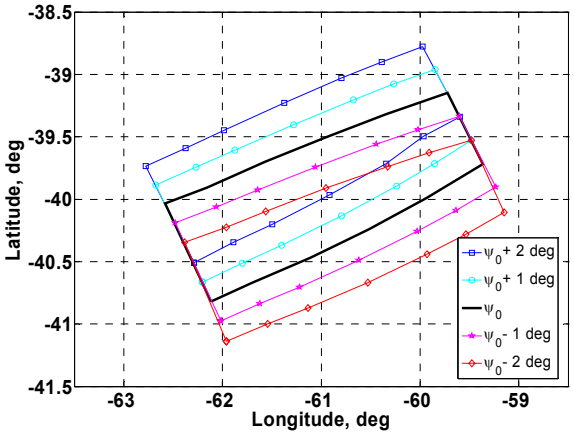

Fig. 10. RFPs for different entry heading angles

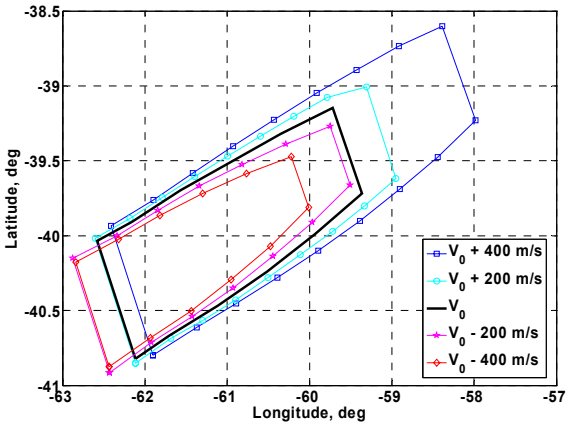

Figure 11. RFPs for varying entry velocities

Changes on the entry velocity also affect the RFP and its characteristics. Fig. 11 shows the RFPs for varying entry velocities. Table 10 shows the size of the RFP for each one of the cases. Increasing V_0 increases the size of the RFP and shifts it further away. Decreasing V_0 shrinks the RFP and brings it closer to the entry point. Fig. 12 shows little influence of V_0 in the deployment altitude. Fig. 13, however, shows how increasing the entry velocity significantly increases the maximum heat rate achieved during entry.

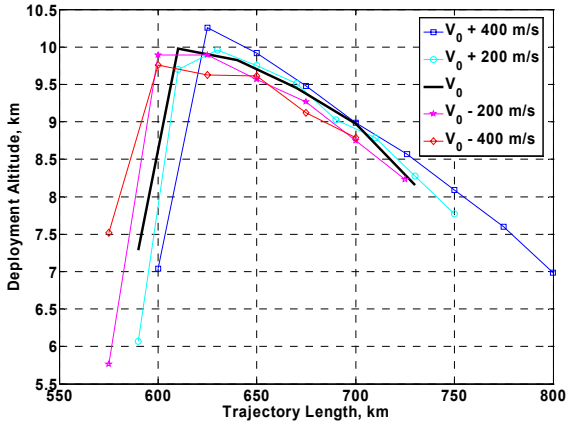

Fig. 12. Deployment altitudes for varying entry velocities

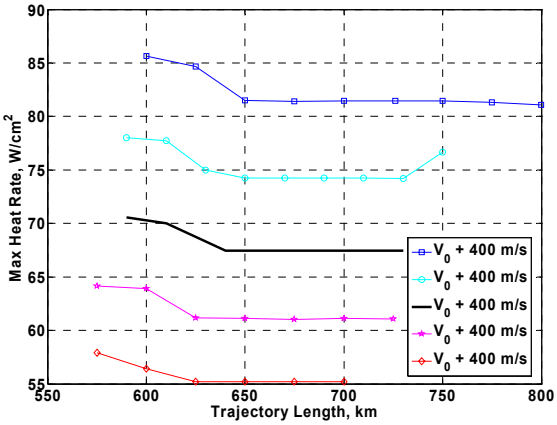

Fig. 13. Maximum heat rate for varying entry velocities

Changes in the entry position, θ_0 and ϕ_0, shift the position of the RFP and have not been studied in this paper. The entry altitude is not changed since it is used as the trigger for the start of entry phase. Now the question becomes: if there is flexibility on where to place the target deployment point, where to put it? Ideally, it should be placed in the center of the footprint, where (i) the deployment altitude in the nominal footprint is the highest and (ii) more dispersions from the nominal entry state can be handled by the entry algorithm. To study (ii) the intersecting region with the above dispersions in the entry state can be computed. Fig. 14 shows the intersecting region of the RFPs generated with $\psi_0 \pm 1$ deg and $\gamma_0 \pm 0.5$ deg. Since changes in V_0 have similar effects to changes in γ_0, it has been ignored for the intersecting region. Fig. 15 shows a view of the nominal RFP and the preferred location of the deployment target. Under nominal conditions, if the target is placed in the preferred zone, an optimal trajectory can be found with dispersions of $\psi_0 \pm 1$ deg and $\gamma_0 \pm 0.5$ deg in the entry state. The larger the dispersions in the entry state are that must be handled, the smaller the preferred zone.

	Length (km)	Width (km)	Area (km^2)
$V_0 + 400\ m/s$	200	56	11200
$V_0 + 200\ m/s$	180	54	9720
V_0	171	51	8721
$V_0 - 200\ m/s$	151	49	7399
$V_0 - 400\ m/s$	126	45	5670

Table 10. Approximate footprint sizes for varying entry velocities

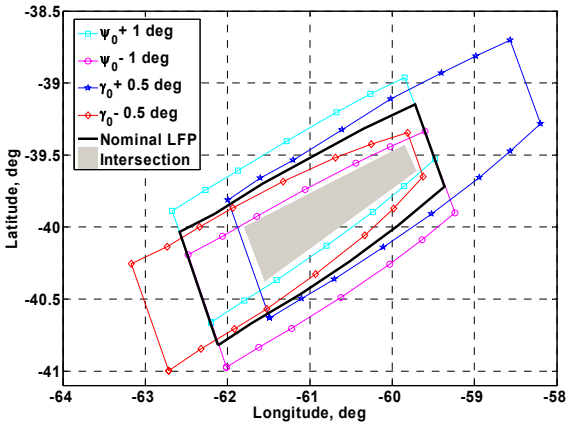

Fig. 14. Intersecting region

For the case presented in this paper, the size of the preferred target location zone is shown in Table 11. The nominal deployment characteristics in the preferred zone would correspond to the characteristics shown in Figs. 3-6 for trajectory lengths between 620 and 720 km.

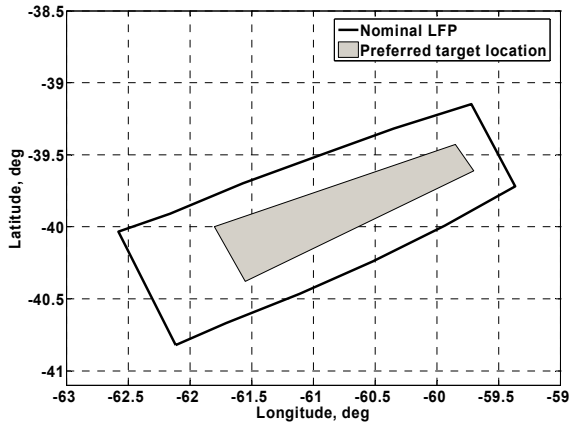

Fig. 15. Zone of preferred target location

	Length (km)	Width (km)	Area (km^2)
Nominal RFP	171	51	8721
Preferred RFP	95	25	2375

Table 11. RFP size

C. Characterization of the RS of a MSL-Type Vehicle for Different Deployment Conditions

For the MSL vehicle and the above nominal entry state the reachable footprints for deployment at Mach 2 and Mach 5 are shown in Fig. 16. The size of the Mach 2 deployment RFP is 171 km in downrange and 51 km in crossrange. For the Mach 5 deployment RFP the size is 111 km in downrange and 36 km in crossrange in the widest part. The RFP for the Mach 5 deployment condition is significantly smaller than the case for Mach 2 deployment condition and hence a smaller set of entry conditions can be accommodated. Fig. 17 shows the deployment altitudes for both Mach 5 and Mach 2 deployment. The deployment altitudes for the Mach 5 deployment are significantly higher than the ones for the Mach 2 condition, and they are higher for the longest trajectories.

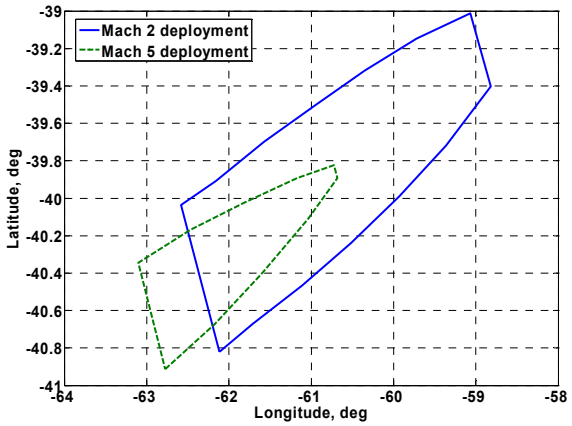

Figure 16. MSL-type vehicle RFPs

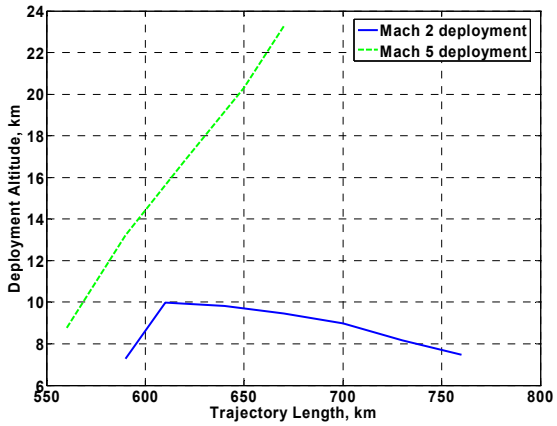

Figure 17. MSL-type vehicle deployment altitudes

Fig. 18 shows the effect of the high deployment velocity on the deployment dynamic pressure. The Mach 5 deployment trajectories which deploy the parachute at low altitudes present very high dynamic pressure. If the deployment dynamic pressure cannot reach high values, the Mach 5 deployment RFP would be reduced in size by discarding the short length trajectories. The Mach 2 deployment dynamic pressures are below 720 Pa, so the deployment conditions are within the limits of the Disk-Gap-Band parachute technology (Table 4).

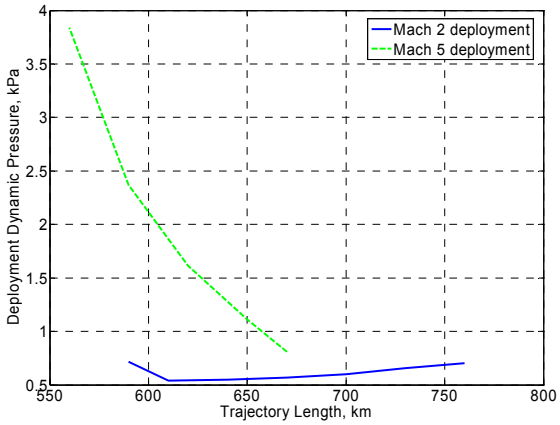

Figure 18. Deployment dynamic pressure

D. Characterization of the RS of a Ellipsled-Type Vehicle for Different Deployment Conditions

For the ellipsled vehicle and the above nominal entry state the reachable footprints for deployment at Mach 2 and Mach 5 are shown in Fig. 19. The size of the Mach 2 deployment RFP is 394 km in downrange and 114 km in crossrange. For the Mach 5 deployment RFP the size is 296 km in downrange and 97 km in crossrange in the widest part. The RFP for the Mach 5 deployment condition is not significantly smaller than the one for the Mach 2 deployment condition. Fig. 20 shows the deployment altitudes for both Mach 5 and Mach 2 deployment. A significant increase in the deployment altitude is observed for the Mach 5 deployment condition.

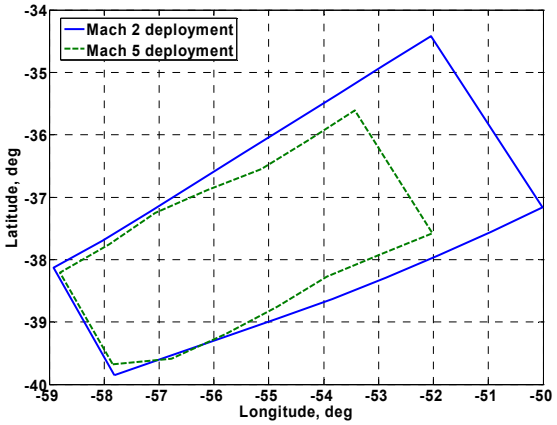

Figure 19. Ellipsled vehicle RFPs

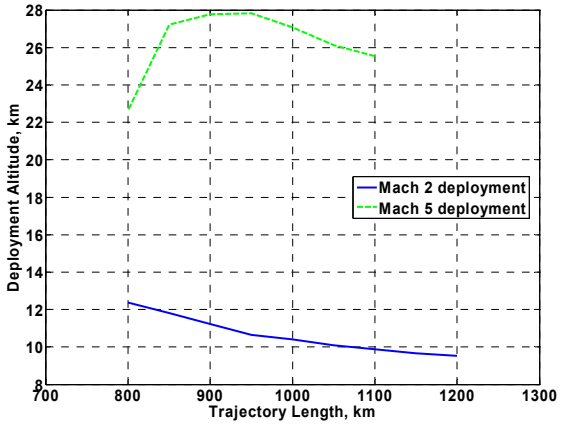

Figure 20. Ellipsled vehicle deployment altitudes

Fig. 21 shows the deployment dynamic pressure. The Mach 5 deployment trajectories which deploy the parachute at lower altitudes present higher dynamic pressure. Since the deployment altitude is higher than for the MSL-type capsule, the deployment dynamic pressure is not as high as the ones shown in Fig. 18. The trajectories with Mach 2 deployment have characteristics within the Disk-Gap-Band parachute limits (Table 4).

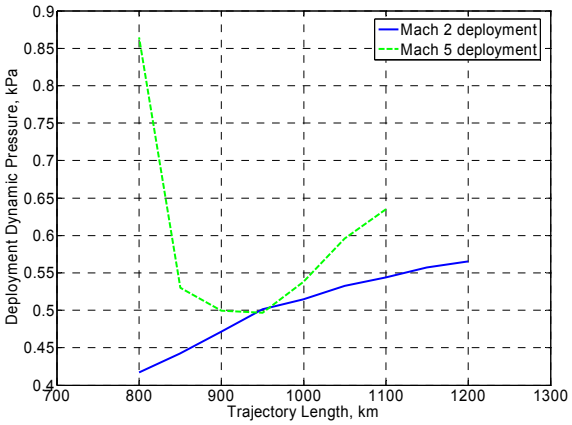

Figure 21. Deployment dynamic pressure

E. Discussion of the Results and Use of the RS in Entry Guidance

From the previous figures, it can be seen how the increased L/D creates a larger RFP, which translates in more landing sites reachable from an entry point and more capability to accommodate entry state dispersions. An increase in L/D also translates into an increased deployment altitude, without any loss of control authority and without an increase in the maximum heat rate reached during entry. Increasing the deployment Mach number reduces the size of the RFP and brings it closer to the entry point (due to the trajectories being shorter) but increases deployment altitude and in some cases increases deployment dynamic pressure substantially.

RSs can be used to evaluate entry guidance algorithms. For the development of guidance algorithms like EAGLE[11], formed by a trajectory planner and a trajectory tracker, the RS can be used to analyze the flexibility and optimality of the trajectory planner. Because the boundaries of the RS are achieved by minimizing or maximizing a function of the final state variables, e.g., downrange, any planner that is not based on solving these trajectory optimization problems will only be capable of planning trajectories to a subset of the RS. How large this subset is relative to the RS is the measure of the planning capability of the planning algorithm; the larger it is, the more entry states that can be accommodated. RS's obtained with a planner can be compared to optimal RS's, as in Ref. 2.

RS's are also used to study the feasibility of a particular nominal entry state. Given the entry state, the planet and vehicle models and a trajectory planner, the nominal RS and the RFP can be computed. The location of the desired deployment point in relation to the RFP provides information about the entry problem. If the deployment point is

outside the footprint, the nominal entry case is infeasible, and at best the algorithm can provide large errors in deployment accuracy. If the desired deployment point is inside the RFP but close to one of the edges of the RFP the nominal entry case is very constrained. In these constrained cases, although a feasible reference trajectory can be planned, in the presence of aerodynamic and/or atmospheric uncertainties, there will be no control left to correct for these uncertainties, and the delivery accuracy will be degraded. Also, since entry state dispersions will move the nominal RFP, if the deployment point is close to the edges, for some of the perturbed entry states the deployment site will fall outside the RFP and become infeasible. Typically the deployment point should be placed in the center of the RFP, to be able to accommodate a larger set of entry dispersions and to leave the trajectory tracker enough control margins to correct for atmospheric and aerodynamic off-nominal conditions and achieve greater deployment accuracy.

V. Controllable Sets

A. Computation of the Controllable Set

Similarly to the computation of the RS explained in the previous section, a subset of the CS is computed via the solution of optimal control problems, this subset will be referred to simply as CS. This section specifies the boundary constraints, the path constraints, the control constraints and the cost function of the optimal problem solved. Table 12 shows the entry boundary constraints for both the MSL-type and the ellipsled-type vehicle. Table 12 also shows the minimum and maximum values of the state variables allowed during entry. The constraint on the maximum radius ensures the trajectories will not skip-out. The CS is computed by fixing the entry velocity and heading angle, and they are assumed they vary around a nominal value. The allowed entry longitudes, latitudes and entry flight path angles will be studied for the given entry velocity and heading angle. Then, the entry velocity and heading angle will be modified around their nominal values to study their impact on the CS.

Table 13 shows the deployment constraints for the MSL vehicle, and Table 14 shows the deployment constraints for the ellipsled vehicle. The deployment states have been obtained from inspecting the RFPs presented in section IV. The deployment trajectory length S_d will be varied until no feasible trajectory is found.

State variable	Nominal entry value for MSL-type vehicle	Nominal entry value for ellipsled-type vehicle	Minimum value	Maximum value	Units
r	3522.2	3522.2	r_p	3522.2	km
θ	Free	Free	-180	180	deg
ϕ	Free	Free	-90	90	deg
V	5433.5 m/s	5650	5800	0	m/s
γ	Free	Free	-45	$\gamma_{\max}$	deg
ψ	15.634524	15.634524	-90	90	deg

Table 12. Entry state constraints

Variable	Value for Mach 2 deployment	Value for Mach 5 deployment	Units
r	$r_p + 8$	$r_p + 16$	km
θ	-61.08	-61.7	deg
ϕ	-40.0	-40.2	deg
V	400	1100	m/s
γ	Free	Free	-
ψ	Free	Free	-
S	S_d	S_d	km

Table 13. Deployment state constraints for MSL-type vehicle

Variable	Value for Mach 2 deployment	Value for Mach 5 deployment	Units
r	$r_p + 11$	$r_p + 25$	km
θ	-54.5	-55.5	deg
ϕ	-37.5	-37.8	deg
V	400	1100	m/s
γ	Free	Free	-
ψ	Free	Free	-
S	S_d	S_d	km

Table 14. Deployment state constraints for ellipsled-type vehicle

The path constraints are shown in Table 12. No constraints in dynamic pressure, heat rate, heat load and total acceleration are imposed, but the values of these variables will be examined. The maximum flight path angle during

entry may be constrained to $\gamma_{\max}$ to ensure the trajectory has enough control authority by avoiding a lofting motion, as explained in Section II.A. For the trajectories presented in this paper $\gamma_{\max}$ is set to $\gamma_{\max} = -1$ deg for all cases.

The CS is obtained by computing the trajectories that form the edges of the CS. The sign of the bank angle is kept constant for each trajectory to form the lateral boundaries of the CS. It is assumed, as with the RS, that the inner points of the CS provide feasible entry trajectories by performing one or more bank reversals during the entry. Two trajectories are computed for a given entry velocity, heading angle, bank sign and trajectory length; one that provides the maximum entry flight path angle and one that provides the minimum entry flight path angle. The maximum and minimum entry flight path angles are obtained by minimizing the cost function shown in Eq. 21.

$$J = k_0 \gamma(0) \tag{21}$$

The value of k_0 is set to $k_0 = 1$ for computing the trajectories with minimum entry flight path angle, and it is set to $k_0 = -1$ for computing the trajectories with maximum entry flight path angle. No term for increasing the control authority is included in the cost function; instead the maximum flight path angle is limited for this purpose.

B. Characterization of the CS of a Nominal MSL-Type Mission

Continuing with the characterization of the nominal MSL mission, with Mach 2 deployment, the CS is presented in this section. Fig. 22 shows the nominal CFP for the minimum entry flight path angle case, which has a length of 1007 km and a width of 212 km in the widest part and 33 km in the narrowest part. The CFP is not symmetric due to the fixed entry heading angle and Coriolis effects. The CFP corresponding to the minimum entry flight path angle is very similar to the one corresponding to the maximum entry flight path angle. The CFP is significantly larger than the RFP because the entry flight path angle is free to take any value. Fig. 23 shows the maximum and minimum entry flight path angles allowed for different trajectory lengths and the maximum heat rate achieved during entry. It is important to see in this figure that if the entry flight path angle is constrained to -15.76793 deg, which is the value used for the initial conditions in the computation of the RFP (Table 6), the trajectory lengths for which there is optimal trajectories is from around 600 km to around 775 km, spanning around 175 km, which is close to the 171 km length of the nominal MSL mission RFP (Fig. 3).

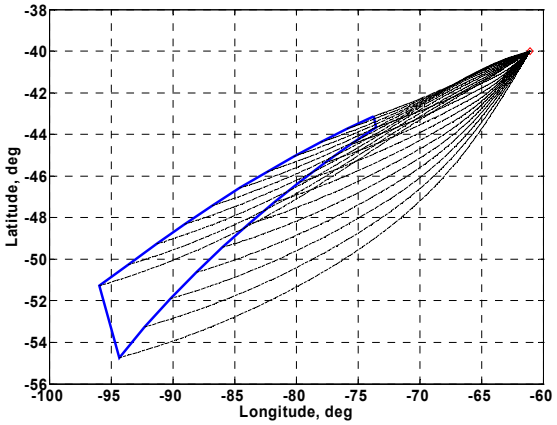

Fig 22. CFP, minimum entry flight path angle

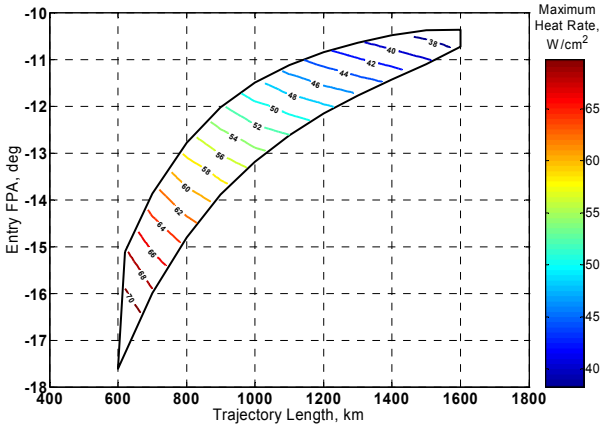

Fig 23. Trajectory length vs. entry flight path angle and maximum heat rate

Fig. 23 also clearly shows how the trajectories with shorter trajectory lengths require steeper entry flight path angles than the ones with longer trajectory lengths, which require much shallower entry flight path angles. The range of acceptable entry flight path angles narrows with increasing trajectory length, from 2.5 degrees for trajectory lengths of 600km to 0.5 degrees to trajectory lengths of 1600 km. The maximum heat rate is increasing for decreasing entry flight path angles and trajectory lengths, as expected, about doubling its value from the maximum trajectory length to the minimum trajectory length. If the maximum heat rate is limited to certain value, due to limits in the Thermal Protection System (TPS), the minimum entry flight path angle and the minimum trajectory length

would be constrained. Fig. 24 shows the total heat load for the different entry flight path angles and trajectory lengths.

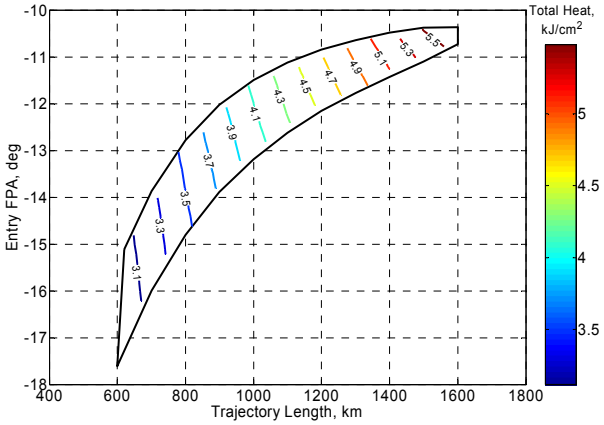

Fig 24. Trajectory length vs. entry flight path angle and total heat load

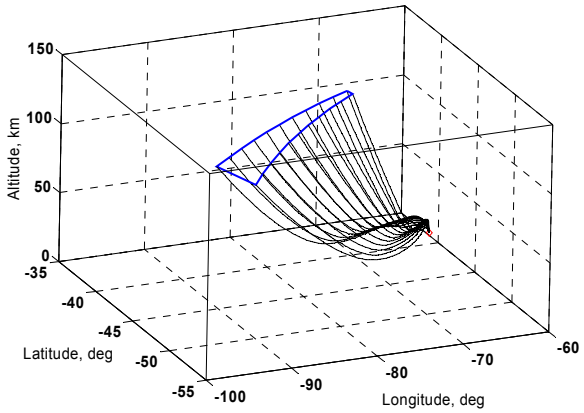

Fig 25. 3D Trajectories for the minimum entry flight path angle case

Fig. 24 shows how the total heat load follows an inverse pattern to the maximum heat rate; the higher the maximum heat rate, the lower the total heat load and vice versa, since the steeper and shorter trajectories are also shorter in time. The TPS limits, then, the range of trajectory lengths and entry flight path angles allowed for entry. The TPS material, which determines the maximum heat rate allowed, will limit the minimum entry flight path angle and minimum trajectory length; the thickness of the TPS, or the TPS mass fraction, determines the maximum heat load allowed, thus limiting the maximum entry flight path angle and maximum trajectory lengths. Fig. 25 shows the 3D trajectories for the minimum entry flight path angle case.

The above plots are computed for a given entry velocity and flight path angle. In order to evaluate the CS, variations in these state variables at the entry interface have to be evaluated. Fig. 26 shows the CFP for different entry velocities, which don't change significantly due to the freedom in the entry flight path angle. It can be seen, however, that lower entry velocities have a CFP that is smaller and closer to the target, and higher entry velocities have a CFP that is larger and further from the target.

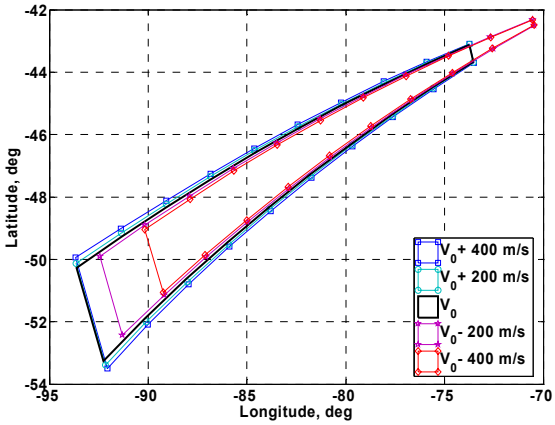

Fig. 26. MSL-type vehicle CFP for variation in the entry velocity

Fig. 27 shows the entry flight path angle profiles for different entry velocities. Note the effect of the entry velocity in the CS. For a given entry flight path angle, the allowed trajectories lengths are shorter for lower entry velocities. Also, for a given trajectory length, the entry flight path angle has to be shallower the lower the entry velocity. Where entry velocity plays a more important role is in the maximum heat rate achieved during entry and the total heat load. Fig. 28 shows the maximum heat rate for different trajectory lengths, entry velocities and entry

flight path angles. The maximum heat rate is higher for higher entry velocities, steeper entry flight path angles and shorter the trajectory lengths.

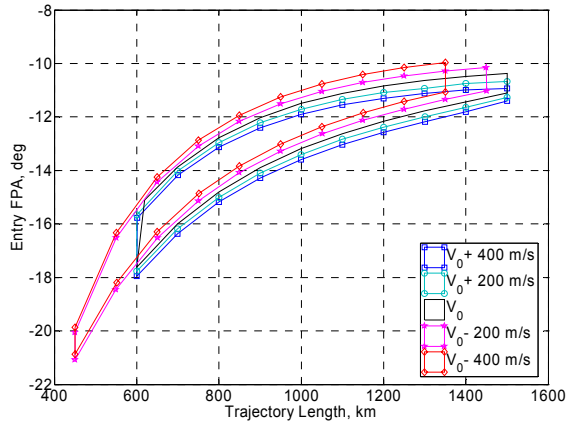

Fig 27. Trajectory length vs. entry flight path angle

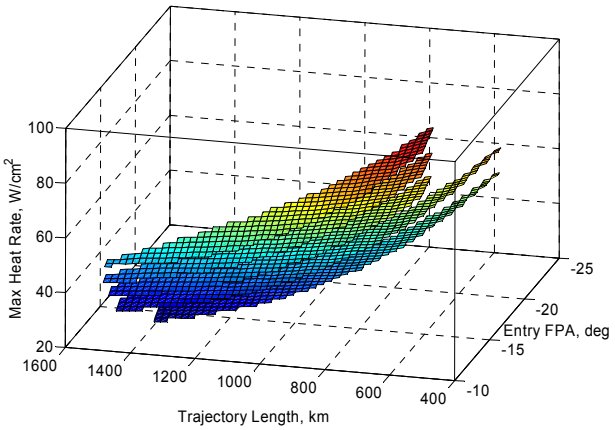

Fig 28. Maximum heat rate with varying entry velocity

Fig. 29 shows the effect of increasing the entry velocity in the total heat load; the higher the entry velocity the higher the total heat load, since the heat rates found in Fig. 28 are also higher. Fig. 30 shows the effect of varying the entry heading in 1 deg steps. Decreased entry heading with respect to the nominal shifts the CFP to the north, and increased entry heading shifts the CFP to the south. This behavior is the opposite of the one shown for the RFP in Fig. 10; since the deployment point is fixed, an increase (decrease) of the entry heading angle shifts the entry point to the south (north).

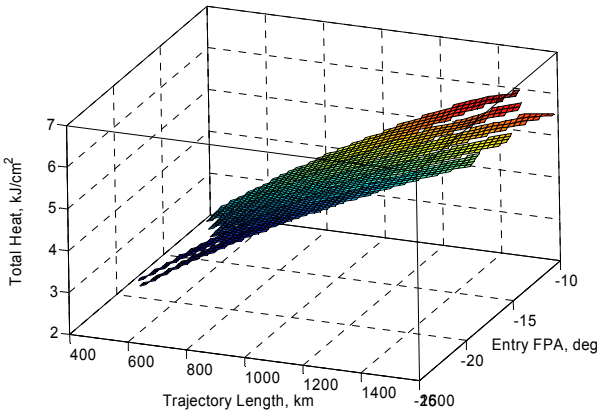

Fig 29. Total heat load for varying entry velocity

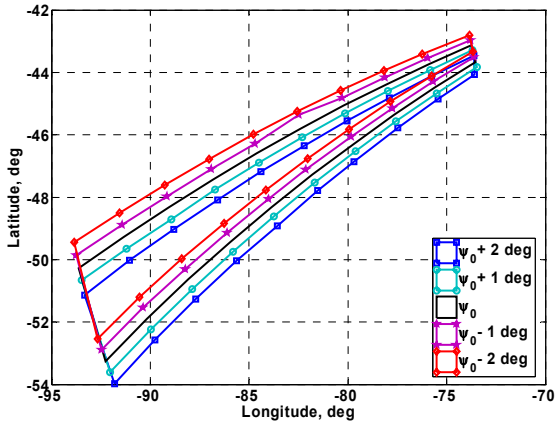

Fig 30. MSL-type vehicle CFP for variation in the entry heading angle

Figures 31-32 show the preferred entry zone for entry dispersions in entry velocity of $\Delta V_0 = \pm 200\, m/s$ and entry heading angle of $\Delta\psi_0 = \pm 1$ deg. These zones have been found by intersecting the plots in Figs. 27 and 30. The larger the entry dispersions that are to be handled, the smaller the preferred entry zone is. Including limits in maximum heat rate and heat load, which are not being imposed in this paper, would reduce the size of the preferred zone.

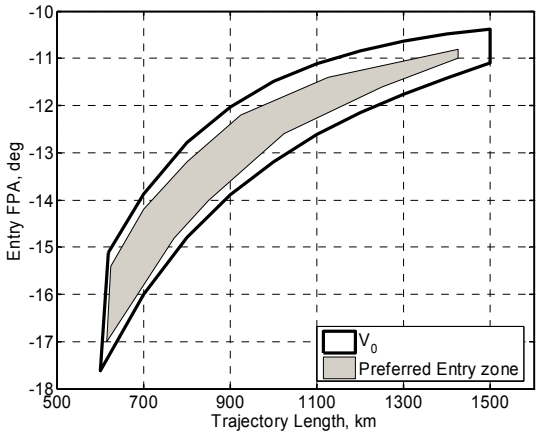

Fig 31. Trajectory length vs. entry flight path angle and preferred zone

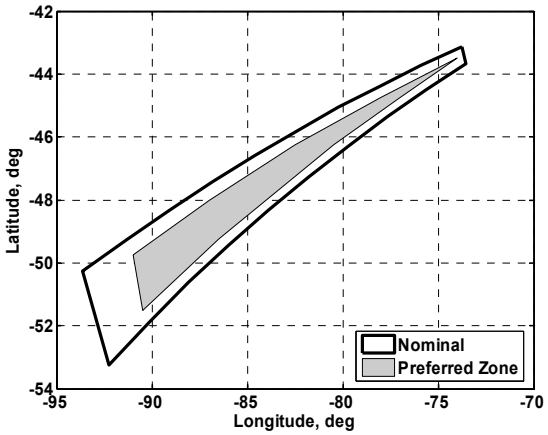

Fig 32. MAS-type CFP and preferred zone

C. Characterization of the CS of a MSL-Type Vehicle for Different Deployment Conditions

For the MSL-type vehicle, the CFPs for the cases of deployment at Mach 2 and Mach 5 are shown in Fig. 33. The dimensions of the Mach 2 deployment CFP are 1029 km long, 211 km wide in the widest part and 32 km wide in the narrowest part. The dimensions of the Mach 5 deployment CFP are 898 km long, 160 km wide in the widest part and 18 km wide in the narrowest part. Fig 34 shows the trajectory lengths vs. the entry flight path angle for both deployment cases.

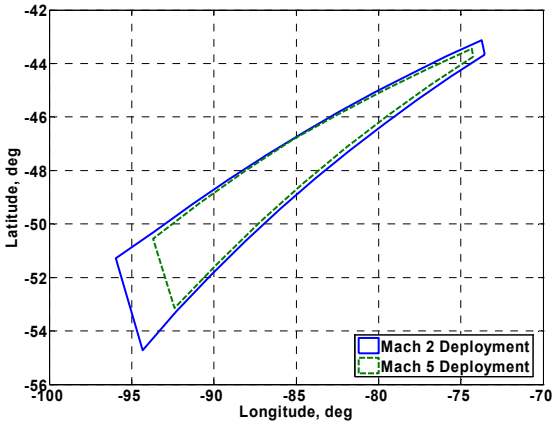

Figure 33. MSL-type vehicle CFP

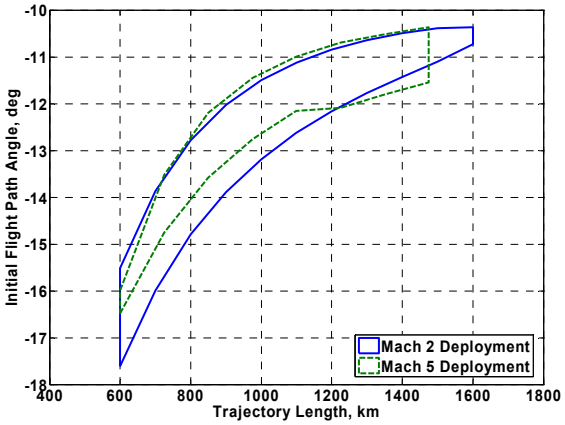

Figure 34. MSL-type vehicle entry flight path angles

Fig. 34 shows how for a fixed entry flight path angle below -13 deg, the CS for the Mach 5 deployment is smaller than for Mach 2 deployment. This characteristic cannot be seen in Fig. 33 due to the freedom in entry flight path angle.

D. Characterization of the CS of a Ellipsled-Type Vehicle for Different Deployment Conditions

For the ellipsled-type vehicle, the CFP for the cases of deployment at Mach 2 and Mach 5 is shown in Fig. 35. The dimensions of the CFP for the Mach 2 deployment conditions are 1039 km long, 316 km wide in the widest part and 52 km wide in the narrowest part. The dimensions of the CFP for the Mach 5 deployment condition are 793 km long, 288 km wide in the widest part and 68 km wide in the narrowest part. Fig. 36 shows the acceptable entry flight path angles for both deployment conditions as a function of the trajectory length.

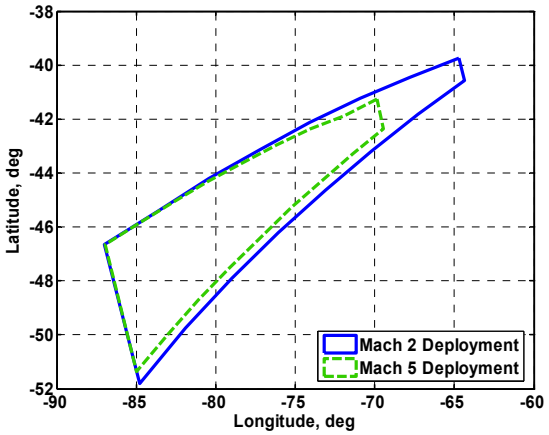

Figure 35. Ellipsled vehicle CFP

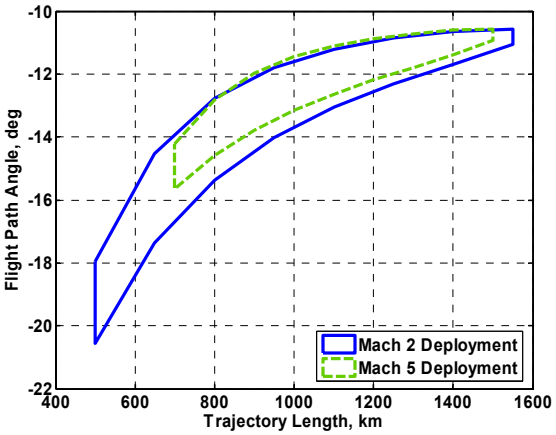

Figure 36. Ellipsled vehicle entry flight path angles

As it can be seen in Fig. 35-36, the increase in deployment velocity reduces the size of the CS, especially the range of allowed entry flight path angles. This effect is greater for the ellipsled vehicle than for the MSL vehicle (comparing Figs. 36 and 34).

E. Discussion of the Results and Use of the CS in Entry Guidance

The results show that increased L/D creates a larger CFP, which translates into more entry sites from which there exists a feasible trajectory to the deployment point. An increase in L/D requires steeper entry flight path angles and hence higher maximum heat rates for a same trajectory length, since the increased L/D makes the vehicle fly higher trajectories with lower drag. Increasing the deployment Mach number reduces the size of the CFP and brings it closer to the deployment point. The increase in deployment Mach number also reduces the allowed entry flight path angles and reduces slightly the maximum heat rates achieved.

The CS can be used to evaluate and design a trajectory planner. The set of entry states from which a planner can construct a trajectory to a designated landing site can be compared to the CS to evaluate the capability of the planner. The evaluation of the planner will depend on the design objectives. In some cases it is desirable for the planner to cover as much of the CS as possible so that large entry state dispersions can be accommodated. In other cases, covering the CS is not important; for example, planning trajectories with high control authority and high deployment altitude may be most important even at the expense of reduced coverage.

Given a nominal entry state, the CFP can be used to evaluate the feasibility of the nominal entry trajectory. The nominal entry case should be chosen, like the deployment point in the RFP, so that it fits far from the boundaries of the CFP (or "in the middle" of the CFP), providing both margins for dispersed entry cases and robustness to modeling errors, leaving control margins to compensate for them and deliver the vehicle with high accuracy.

VI. Conclusions

As means of characterizing the envelope of entry trajectories for a given vehicle, we have defined reachable and controllable sets and the related reachable and controllable footprints. The sets were used to characterize the Mars entry problem with special attention to high altitude parachute deployment and high control authority trajectories. It was shown how these sets can be used to design and evaluate entry guidance algorithms and how they can be used to specify a nominal entry state and a nominal parachute deployment site.

Although the illustrations in this paper were limited to Mars entry, reachable and controllable set analysis is applicable to entry at Earth and other atmosphere-bearing planets and satellites. For example, the new crew exploration vehicle, Orion, will be required to bring safely the crew to a designated landing site with high accuracy, without violating the restrictive crew and vehicle constraints and being able to accommodate a high number of different entry conditions[12]. In the case of a return from the Moon, it will be needed to accommodate trajectories with very different downranges, from 3100 to 5400 nmi, which will require skip-entry trajectories. The controllable set to a designated landing site can be used to evaluate the capability of an entry algorithm to accommodate the downrange requirements. Entry from low earth orbit (from the International Space Station for instance) will require handling abort and emergency scenarios as autonomously as possible, for which the computation of the RS can be used to select the landing site among all the ones reachable from the vehicle's entry position.

Acknowledgments

The research reported in this paper was sponsored by the Jet Propulsion Laboratory, California Institute of Technology under contract with the National Aeronautics and Space Administration.

References

[1]Sontag, E.D., "Mathematical Control Theory," 2nd ed., Springer, New York, 1998.

[2]Saraf, A., Leavitt, J. A, Ferch, M., and Mease, K. D., "Landing Footprint Computation for Entry Vehicles," AIAA Paper 2004-4774, August 2004.

[3]Braun, R.D. and Manning, R. M., "Mars exploration entry, descent, and landing challenges," J. Spacecraft and Rockets, vol. 44, no. 2, pp. 310–323, 2007.

[4]J. Benito, and K. Mease, "Entry Trajectory Planning For Higher Elevation Landing," AAS Paper 07-309, AAS/AIAA Astrodynamics Specialist Conference, Mackinac Island, MI, August 2007.

[5]J. Boada, J. Benito and K. D. Mease, "Near Optimal Planner for Higher Elevation Landing," 2008 Pegasus-AIAA Student Conference, Prague, Czech Republic.

[6]GESOP - Graphical Environment for Simulation and Optimization, http://www.gesop.de/

[7]Vinh, N. X., "Optimal Trajectories in Atmospheric Flight," Elsevier, New York, 1981.

[8]Lockwood, M. K., Sutton, K., Prabhu, R., and Powell, R. W., "Entry Configurations and Performance Comparisons for the Mars Smart Lander," AIAA Paper 2002-4407, AIAA Atmospheric Flight Mechanics Conference & Exhibit, Monterey, CA, August 2002.

[9]Sutton, K., and Graves, R., "A General Stagnation-Point Convective-Heating Equation for Arbitrary Gas Mixtures," NASA TR R-376, 1971.

[10]Witkowski, A., and Brown, G., "Mars Deployable Decelerators Capability Roadmap Summary," 2006 IEEE Aerospace Conference, Big Sky, MT, Inst. of Electrical and Electronics Engineers, Paper 1585, March 2006.

[11]Saraf, A., Leavitt, J. A., Chen, D. T., and Mease, K. D., "Design and Evaluation of an Acceleration Guidance Algorithm for Entry," Journal of Spacecraft and Rockets, Vol. 41, No. 6, 2004, pp. 986–996.

[12]Broome, J. and Johnson, W., "Orion Entry, Descent, and Landing Performance and Mission Design," AIAA Paper 2007-6430, AIAA Guidance, Navigation and Control Conference and Exhibit, Hilton Head, SC, August 2007.